Ceramics International 50 (2024) 36295–36305

Contents lists available at ScienceDirect

Ceramics International

journal homepage: www.elsevier.com/locate/ceramint

Cluster/shell citrate-Fe_3O_4/chitosan nanoparticles for enhancing heating efficiency in combined magnetic and photothermal therapy

Gracia García-García [a,b,*], Marina Lázaro [c], Alejandro Cenalmor [d], Isabel García-Álvarez [d], Guillermo R. Iglesias [c,e], José L. Arias [e,f,g]

[a] Department of Nursing, Physiotherapy and Medicine, Faculty of Health Sciences, University of Almería, Almería, Spain
[b] Biomedical Research Unit, Torrecárdenas University Hospital, 04009, Almería, Spain
[c] NanoMag Lab. Department of Applied Physics, Faculty of Science University of Granada, Planta -1. Edificio I+D Josefina Castro, Av. de Madrid, 28, 18012, Granada, Spain
[d] Facultad de Ciencias Experimentales, Universidad Francisco de Vitoria, Pozuelo de Alarcón, 28223, Madrid, Spain
[e] Biosanitary Research Institute of Granada (ibs.GRANADA), Andalusian Health Service (SAS), University of Granada, 18001, Granada, Spain
[f] Department of Pharmacy and Pharmaceutical Technology, Faculty of Pharmacy, University of Granada, 18071, Granada, Spain
[g] Institute of Biopathology and Regenerative Medicine (IBIMER), Center of Biomedical Research (CIBM), University of Granada, Av. del Conocimiento, 18016, Granada, Spain

ARTICLE INFO

Handling Editor: Dr P. Vincenzini

Keywords:
C. Magnetic properties
C. Thermal properties
B. Nanocomposites
D. Biomedical applications

ABSTRACT

Antitumor hyperthermia therapy is an emerging approach for the thermal treatment of cancer. Magnetite-based nanoparticles are very promising hyperthermia agents due to its biocompatibility and versatile application. In this study, engineered citrate functionalized magnetite nanoparticles resulted in an adequate colloid for the desire application: 12.57 nm ± 3.86, −44.5 ± 0.6 mV, hydrophilic character, and 85.2 ± 1.6 emu/g. Those citrate-functionalized magnetite colloids were embedded into a chitosan nanomatrix to obtain cluster/shell citrate-magnetite/chitosan nanoparticles with demonstrated short-term stability. In addition, freeze-drying using saccharose as cryoprotectant was used for a long-term preservation. Cluster/shell nanostructure was confirmed using Fourier transform infrared spectroscopy, X-ray diffraction analysis, thermogravimetric analysis, surface electrokinetics and thermodynamics, dynamic light scattering and high resolution transmission electron microscopy. Citrate-magnetite/chitosan nanoparticles demonstrated negligible cytotoxicity in a non-tumor cell line and adequate characteristics for parenteral administration (187.33 ± 54.85 nm and haemocompatibility). Magnetic behaviour was not affected by the chitosan shell onto the citrate-magnetite cluster of particles. Thermal enhance capacity was fully investigated using magnetic hyperthermia and photothermal modalities. Specific absorption rate values resulted for citrate-magnetite/chitosan NPs were superior to that obtained for single core particles in magnetic hyperthermia (393 ± 45 and 239 ± 31) and photothermal therapy (384 ± 7.1 and 272 ± 0.8, respectively). Therefore, citrate-magnetite/chitosan cluster/shell nanoparticles could find antitumor hyperthermia applications by using a systemic a dual magneto-photo-thermal therapy.

1. Introduction

In the 19th century, fever observed in cancer patients after the administration of living bacteria was related to partial tumor regression. Since then, interest in antitumor thermal treatments, also known as antitumor hyperthermia, has increased significantly. In recent decades, significant efforts have been made to understand the mechanisms of antitumor hyperthermia therapy, resulting in a complex combination of approaches that can act at both cellular and tissue levels. Thermal treatments and their effects on tumors can be classified based on the magnitude of the induced temperature increment. Irreversible injury treatments above 48 °C involve coagulative necrosis, resulting in non-selective cell death that has no interest in anticancer treatments. Selective cell necrosis can be achieved between 48 and 45 °C. From 39 to 45 °C, protein denaturation and oxidative stress can lead to cellular damage, mainly via apoptosis [1]. Combining cellular death induced by

* Corresponding author. Department of Nursing, Physiotherapy and Medicine, Faculty of Health Sciences Universidad de Almería, 04120, La Cañada, Almería, Spain.
E-mail address: graciagg@ual.es (G. García-García).

https://doi.org/10.1016/j.ceramint.2024.07.013
Received 3 April 2024; Received in revised form 20 June 2024; Accepted 2 July 2024
Available online 2 July 2024

thermal treatments with radiotherapy and some chemotherapeutic agents has shown to be more effective [2,3]. Interestingly, a body temperature increment to 41 °C is also associated with blood flow enhancement, which may contribute to a low resistance appearance of chemotherapy and immunotherapy, especially in poorly or heterogeneously vascularized tumors [3,4].

In addition to a deeper understanding of the mechanisms underlying hyperthermia, recent advances in heating methods have enabled its clinical application. This scientific progress has been made possible thanks to the substantial progress in the nanotechnology field and its contribution to the engineering of nanoparticle (NP)-based strategies for remote and localized heating [5]. Metallic and magnetic NPs are used as hyperthermia agents due to their physicochemical properties at the nanoscale, for photothermal therapy (PTT) and magnetic hyperthermia (MHT), respectively. PTT is based on the plasmonic photothermal phenomena, where the heat release results from the interaction of near-infrared (NIR) light with electrons movement on the metallic surface. Among various metallic NPs, gold NPs are the most investigated in preclinical research due to their outstanding heating capacity. Despite efforts to understand their biocompatibility, there are still concerns about their potential toxicity at the doses required for antitumor PTT [6]. In MHT, when magnetic NPs behave as single dipoles and are exposed to an alternating magnetic field (AMF), they can be reoriented. Subsequent relaxation, either through Brownian or Néel relaxation, results in heating dissipation. Iron oxide NPs are the most relevant magnetic NPs, and they have been approved for human use as therapeutic in antitumor MHT for patients with recurrent glioblastoma (Nanotherm®) due to their magnetic characteristic and extensive biocompatibility at sizes below 50 nm [7]. It is noteworthy that its clinical use is limited to accessible tumors, as temperatures required for hyperthermia can only be achieved by intratumoral administration injection of iron oxide NPs [8].

MH and PTT were considered as two distinct approaches for antitumor hyperthermia therapy, until recently, when photothermal properties of iron oxide NPs, concretely magnetite (Fe_3O_4), have been reported [9–11]. In 2016, Espinosa et al., reported a dual magneto-photo-thermal therapeutic strategy based on the intratumoral administration of iron oxide NPs as heating agents, which demonstrated superior antitumor effects compared to both MHT and PTT modalities used independently [12]. Thus, the engineering of a novel generation of iron oxide-based nanoparticles for dual magneto-photo-thermal antitumor therapy holds significant promise in optimizing antitumor hyperthermia therapy [13].

Chitosan (CS), a cationic polysaccharide resulting from the N-deacetylation of chitin, is an attractive candidate for biomedical applications because of its high biocompatibility, as well as other multiple functionalities. This polymer has been used in the preparation of targeted NPs due to its appropriate chemical structure for thermo- and pH-responsive and ligand functionalization [14]. For the systemic administration of NPs, CS could be used for the surface decoration of NPs as a promising strategy for the formulation of systemic stealth NPs with an elongated blood circulation half-time, as it has been reported from some of us [15]. In addition, this polymer has been extensively used for the stabilization of magnetic NPs for MH purposes [16–19].

The design of cluster/shell nanostructures, where iron oxide particles form the cluster and polymeric materials serve as the shells offers several advantages such as targeted delivery, controlled drug release, higher colloidal stability and biocompatibility as it has been reported by some of us [20–23]. For magnetic properties optimization, clusters or aggregates of magnetics NPs display a significantly enhanced magnetic properties than the monodisperse NPs. This strategy has been previously reported for the synthesis of magnetic nanosensors based on their T_2-weighted MRI signals alterations [24], and as a systemic administration approach for antitumor MH [25]. In addition, it has been reported that *in vivo* intratumoral administration of ligand-induce aggregation of single iron oxide NPs can enhance thermal increase via PT [26].

In this context, it is important to develop a safe and effective therapeutic approach for applying NP-mediated hyperthermia to tumors that are inaccessible via local injections. Herein, we report the development of cluster/shell citrate cit-Fe_3O_4/CS NPs, along with a broad chemical and physical characterization. Stability of the cit-Fe_3O_4/CS NPs has been deeper assessed through freeze-drying procedure and in biological media (PBS). In addition, an *in vitro* biocompatibility and a haemocompatibility evaluation has been performed. We thoroughly assessed the potential use of CS as a hyperthermia based-NPs adjuvant when it constitutes a nanoshell for cit-Fe_3O_4 particles cluster in MH and PT. Therefore, a comprehensive *in vitro* study has been performed with high potential and safety for future parenteral administered *in vivo* models for antitumor therapy. To our knowledge, this is the first time that magnetic clustering has been performed using a CS polymeric coating. This strategy is promising not only because it could enhance magnetic properties and magnetic hyperthermia potential, but also because it can improve optical properties, and so, photothermal therapy efficiency. Hence, the use of cit-Fe_3O_4/CS NPs may be a promising strategy for the clinical translation of photothermal therapy. We believe that this novel nanostructure could be considered as an example of a new generation of systemic administered dual magneto-photo-thermal antitumor nanomaterials.

2. Materials and methods

2.1. Materials

Iron (III) chloride hexahydrate ($FeCl_3{\cdot}6H_2O$, M_W: 270.32 g/mol), iron (II) chloride tetrahydrate ($FeCl_2{\cdot}4H_2O$, M_W: 198.81 g/mol), potassium nitrate (KNO_3, M_W: 101.10 g/mol), perchloric acid ($HClO_4$, 70 %, M_W: 270.30 g/mol), hydrochloric acid (HCl, 37 %, M_W: 36.46 g/mol), and acetic acid (CH_3COOH, M_W: 60.05 g/mol, ≥98 %) from VWR International, LLC (Spain). Low M_W CS (from 50 to 190 kDa, determined by viscosity measurement; polydispersity not determined by the laboratory; 75–85 % deacetylated; 99 % purity level), sodium citrate ($Na_3C_6H_5O_7$, M_W: 258.07 g/mol, anhydrous, ≥98 %), sodium hydroxide (NaOH, M_W: 39.99 g/mol), formamide (CH_3NO, Mw: 45.04 g/mol, ≥99 %), diiodomethane (CH_2I_2, Mw: 267.84), ethylenediaminotetraacetic acid (EDTA, $C_{10}H_{14}N_2Na_2O_8{\cdot}2\ H_2O$, Mw: 372.24 g/mol), phosphate buffered saline (PBS), and calcium chloride dihydrate ($CaCl_2{\cdot}2H_2O$, Mw: 147.01 g/mol) were obtained from Merck KGaA (Germany). Kolliphor® P-188 from BASF (Germany). Saccharose from ACROS Organics™ (Belgium). Ammonia (NH_3, 30 %, M_W: 17.03 g/mol, ACS specification) from Panreac (Spain). Sodium sulfate anhydrous (Na_2SO_4, M_W: 142.04 g/mol) from Guinama S.L. (Spain). Ammonium oxalate monohydrate ($C_2H_{10}N_2O_5$, Mw: 142.111 g/mol, ≥98 %) and Triton® X-100 from ThermoFisher Scientific Inc. (USA). Human P-Selectin/CD62P Quantikine ELISA Kit from rndsystems (USA). Human C3a ELISA Kit (BD OptEIA™ Human C3a ELISA Kit) from bdbiosciences (USA). 3-(4,5-dimethylthiazol-2-yl)-2,5-diphenyltetrazolium (MTT, Merck Millipore, Germany), Dulbecco's Phosphate Buffered Saline (DPBS), Dulbecco's High Glucose Modified Eagle's Medium (DMEM) with and without Phenol Red, Fetal Bovine Serum (FBS) (Gibco™, Thermo Fisher Scientific, Spain); L-glutamine saline solution (200 mM), penicillin- (10.000 U/mL)/streptomycin (10.000 μg/mL)/amphotericin B (25 μg/mL) solution (100 × , Merck Millipore, Germany). Water was deionized and filtered with a Milli-Q Academic®, Millipore, France. All chemicals were of analytical quality.

2.2. Methods

2.2.1. Nanoparticle engineering procedure

2.2.1.1. Synthesis and surface functionalization of the Fe_3O_4 colloids.

Fe_3O_4 colloids were synthesized by a chemical co-precipitation methodology [20]. Briefly, 40 ml of 1 M $FeCl_3$ and 10 ml of 2 M $FeCl_2$ and 2 M HCl were simultaneously poured to 500 ml of 0.7 M NH_3 under mechanical stirring. Resultant particles were magnetically isolated and incubated in 250 ml 2 M $HClO_4$ solution overnight. Finally, the magnetic particles underwent repeated centrifugation cycles (40 min at 8500 g) and were redispersed in Milli-Q water until the supernatant conductivity was ≤50 μS/cm.

To obtain cit-Fe_3O_4 resultant Fe_3O_4 colloids in a 0.1 N citrate solution were sonicated for 30 min. Then, the pH was adjusted to 7 using a 0.5 M NaOH solution [27]. The resultant dispersion underwent repeated centrifugation cycles (40 min at 8500 g), with pellets being redispersed in Milli-Q water until the supernatant conductivity was ≤10 μS/cm.

2.2.1.2. Preparation of the CS and the cit-Fe_3O_4/CS cluster/shell NPs. CS and cit-Fe_3O_4/CS cluster/shell NPs were engineered using the CS coacervation procedure with some modifications [21,28]. For that, a solution of 0.05 w/v CS (2 %, v/v acetic acic) and 1 %, w/v Kolliphor® P-188 in 25 ml was prepared, with cit-Fe_3O_4 added in a 1:1 cit-Fe_3O_4:CS ratio. Coacervation of the CS nanoshell was induced by adding dropwise a 6.25 ml 20 % w/v Na_2SO_4 solution under sonication using a Branson Sonifier 450 sonication probe (Emerson Electric Co., USA) (Fig. 1). Subsequently, magnetic isolation of the cit-Fe_3O_4/CS NPs was performed to ensure a conductivity of ≤10 μS/cm.

The NPs production yield was determined in triplicate as followed (Equation (1)):

Yield (%) = [cit-Fe_3O_4/CS NPs obtained (mg)/ total materials used in the CS coating (mg)] (1)

2.2.1.3. Lyophilization of cit-Fe_3O_4/CS cluster/shell NPs. Resultant cit-Fe_3O_4/CS NPs (0.25 mg/mL) were freezed at −80 °C during 24 h in presence or absence of saccharose used as lyoprotectant (5 %, w/v; n = 3). Lyophilization was performed for 48 h in a Telstar LyoQuest55 (Telstar®, Spain). Then, samples were storage at 20 °C during a month. Lyophilized cit-Fe_3O_4/CS NPs dispersed in water at the target concentration for further analysis.

To remove saccharose from the cit-Fe_3O_4/CS NPs freeze-dried in its presence, they were redispersed in water (1 mg of NPs in 5 ml of water) and then, subjected to three magnetic isolation steps. After each magnetic isolation step, an equal volume of water was added, and the NPs were sonicated 15 min. Then, the evaluation of the particle sized in terms of DLS and surface electrical charge in terms of ζ values was tested.

2.2.2. Characterization of cit-Fe_3O_4/CS NPs

2.2.2.1. Dynamic and electrophoretic light scattering evaluation. Dynamic light scattering (DLS) analysis was used to evaluate hydrodynamic size (and polydispersion or PdI) while electrophoretic light scattering techniques was performed to determine zeta potential (ζ) values of the particles (n = 9). Samples measurements (0.1 %, w/v NPs dispersion in water) were done at 25.0 ± 0.1 °C using a Zetasizer Nano-ZS, Malvern Instruments Ltd., United Kingdom at a scattering angle of 90°. Cit functionalization of Fe_3O_4 and CS coating onto the cit-functionalized Fe_3O_4 was qualitatively evaluated by determining the influence of pH (pH values from 3 to 9, in the presence of 10^{-3} M KNO_3) and the ionic strength (fixed with KNO_3 concentrations up to 0.1 M) on the ζ values of Fe_3O_4, cit-Fe_3O_4, CS and cit-Fe_3O_4/CS NPs. Prior to measurements, NPs were incubated within the dispersion media under mechanical stirring (150 rpm, Boeco universal orbital shaker OS-10, Boeco, Germany) during 12 h.

Colloidal stability of the cit-Fe_3O_4/CS NPs in Milli-Q water and in media physiologically relevant condition for biomedical application [phosphate buffered saline (PBS)]. It was investigated by the determination of ζ values and DLS analysis according to Equation (2), where t_1 represents the time duration for assessment (1 week) [29].

Colloidal stability at t_1 = cit-Fe_3O_4/CS NPs size at t_1 / initial cit-Fe_3O_4/CS NPs size (2)

2.2.2.2. High resolution electron transmission microscopy analysis. High

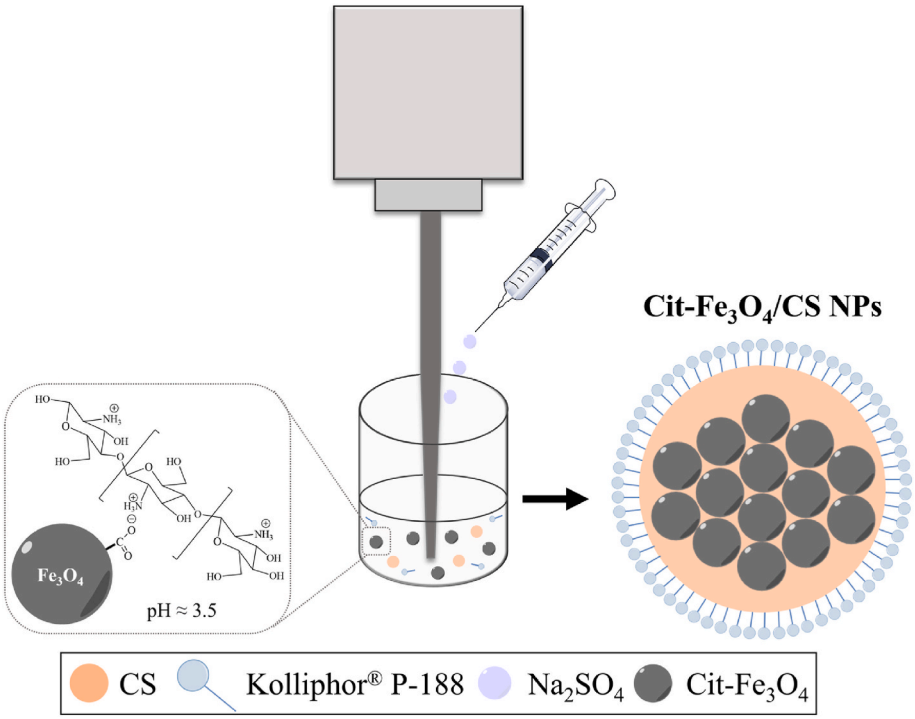

Fig. 1. Engineering of cit-Fe_3O_4/CS NPs by coacervation methodology.

resolution transmission electron microscopy (HRTEM) was also used to analyze structure of the cit-Fe_3O_4, cit-Fe_3O_4/CS and lyophilized cit-Fe_3O_4/CS in the presence of 5 % w/v saccharose NPs (Titan G2 60–300 FEI microscope, Thermofisher Scientific Inc., USA; accelerating voltage of 200 kV). Prior to observation, a drop of the NPs dispersion (0.1 %, w/v) was poured to a formvar/carbon-coated copper microgrid, and then dried under 25.0 ± 0.5 °C. The sizes were measured using ImageJ software (freeware from the National Institute of Health) and, then, used to calculate particle size distribution.

2.2.2.3. Thermogravimetric, Fourier transform infrared and X-ray diffractometry analysis. Thermogravimetric analysis (TGA) of cit-Fe_3O_4 and cit-Fe_3O_4/CS samples was performed under 50 mL/min N_2 flow with a heating rate of 10 °C/min (TGA-50H SHIMADZU, Japan).

Structure of cit-Fe_3O_4/CS NPs was confirmed by Fourier transform infrared (FTIR) spectroscopy (FT/IR-6200 spectrometer JASCO, United States; resolution of 0.25 cm^{-1}). Fe_3O_4, cit-Fe_3O_4 and CS NPs were used as controls.

Mineralogical purity and crystallinity of the Fe_3O_4 nuclei in the cit-Fe_3O_4/CS NPs was evaluated by means of X-ray diffractometry (XRD) analysis (BRUKER D8 DISCOVER, PILATUS3R 100K-A, Cu-Kα radiation, λ = 1.5405 Å).

2.2.2.4. Surface-free energy evaluation. Surface-free energy evaluation was performed by using the van Oss model [30], highly suitable for colloids surface thermodynamic analysis [31,32]. The followed methodology has been previously described [20,33]. Briefly, contact angles (θ) of microdroplets (4 μl, Gilmont micrometer syringe, Gilmont, Gilmer, United States) of three selected liquids (water, formamide, and diiodomethane) were measured on the samples. Measurements were done in a thermostatic chamber at 25.0 ± 0.1 °C using a telegoniometer (Ramé-Hart 100-00 telegoniometer, Ramé-Hart, Succasunna, United States). Pretreatment of the samples consisted of the preparation of a homogenized and dried layer of each nanomaterial (cit-Fe_3O_4, CS and cit-Fe_3O_4/CS).

2.2.2.5. Magnetic properties. Magnetization cycle of cit-Fe_3O_4 and cit-Fe_3O_4/CS NPs were performed at room temperature (20 °C ± 0.5 °C) using an inductive magnetometer AC Hyster Series magnetometer (Nanotech Solutions S.L., Madrid, Spain). The magnetometer operates at a frequency of 1.5 kHz and a field strength of 120 kA/m. All the magnetization values (in emu/g) were normalized in terms of sample Fe concentration.

The magnetic field responsive behaviour of 0.5 % (w/v) aqueous dispersions of cit-Fe_3O_4 and cit-Fe_3O_4/CS NPs was qualitatively analysed by optical visualization using a permanent magnet.

2.2.3. Thermal measurements

2.2.3.1. Magnetic hyperthermia analysis. MHT measurements were performed in Eppendorf tubes containing 0.5 ml NPs (cit-Fe_3O_4 NPs and cit-Fe_3O_4/CS NPs) in a concentration of 5 mg/ml. The AMF was generated from a 6-turn coil of 4 mm inner copper tube (45 mm length, 20 mm inner diameter) connected to an AC current generator system [34]. To ensure that the temperature increase was only a result from the MH effect, a thermostatic water bath was using during the whole length of the experiment (25.0 ± 0.5 °C). The frequencies used varied from 120 to 190 kHz, with a magnetic field strength of 16 kA/m measured using a magnetic sensor probe (NanoScience Laboratories Ltd. UK). Temperature was recorded at 3 s time intervals using an optical fiber thermometer (Optocon AG, Weidmann Technologies Deutschland GMBH, Germany).

2.2.3.2. Photothermal measurements. Assay of the PT capacity of the NPs (cit-Fe_3O_4 NPs and cit-Fe_3O_4/CS NPs) was performed by using a NIR laser of 850 nm wavelength at 0.1, 0.5 and 1 W/cm^2. Eppendorf tubes containing 0.5 ml NPs (cit-Fe_3O_4 NPs and cit-Fe_3O_4/CS NPs) with a concentration of 5 mg/mL. Temperature was measured and recorded by a thermographic camera (Flir 60 with 320 × 240 pixels, IR resolution, and thermal sensitivity of 0.045 °C; FLIR Systems, Inc., USA).

2.2.3.3. Specific absorption rate evaluation. The Specific Absorption Rate (SAR) is a measure of how much heat per unit mass is generated by the NPs and is experimentally calculated with Equation (3):

$$SAR = \frac{C_{liq}\rho_{liq}}{\varphi}\frac{dT}{dt} \quad (3)$$

being C_{liq} the mass specific heat, ρ_{liq} is the density of the suspension and φ is the mass concentration of NPs and dT/dt. It is also determined by the rate at which the temperature of the sample increases (dT/dt) as a function of time. For the MHT determination, Box-Lucas phenomenological model is used, and in PTT we will use the linear fit to the first 30 s of temperature increase [35].

2.2.4. Cytotoxicity assay of the cit-Fe_3O_4/chitosan cluster/shell nanoparticles

Cell cytotoxicity of the cit-Fe_3O_4/CS NPs was assessed as previously reported [36]. Briefly, BV2 microglia cells were grown in a 96-well plate (7.500 cells per well) during 24 h. Cells were exposed to different concentrations of the cit-Fe_3O_4/CS NPs (10–200 μg/ml) and incubated for another 24 h. Cell viability was measured with the MTT assay, as previously described [36].

2.2.5. Haemocompatibility of the cit-Fe_3O_4/chitosan cluster/shell nanoparticles

Blood potential interactions with developed cit-Fe_3O_4/CS NPs were tested to evaluate the NPs feasibility in biomedical applications. Blood aliquots were collected from two healthy female adults (24 and 45 years old) and incubated with cit-Fe_3O_4/CS NPs for the assessment of haemolysis, coagulation and complement system activation when comparing with PBS as negative control ($n = 3$). A previously detailed methodology suitable for NPs heamocompatibility determination was followed [22,37].

2.2.6. Statistical analysis

Cytotoxicity assays were performed in triplicates per experimental condition. Data are presented as mean ± standard error of the mean (SEM), of at least three independent experiments. Statistically significant differences between multiple groups were determined by Kruskal–Wallis test. All statistical analysis were performed using GraphPad Prism (version 9.0, USA).

3. Results

3.1. Characterization

3.1.1. Particle size and surface electrical charge

Fe_3O_4 and cit-Fe_3O_4 particle size determined by DLS was found to be 68 ± 20 and 42 ± 15 nm, respectively. Cit functionalization of Fe_3O_4 is an extended methodology used for the obtention of sterically stabilized Fe_3O_4. Such stabilization is probably the reason why the size decrease in terms of hydrodynamic size [27,38,39]. The strong electrostatic repulsion forces between the cit-Fe_3O_4 particles within the dispersion medium, compared to the non-functionalized Fe_3O_4, could also be demonstrated by the surface electrical charge, as greater absolute ζ values were noticeable [40] (Table 1). Therefore, both DLS and electrophoretic light scattering analysis were of great value for investigating colloidal stability, consistent with previous research [41,42]. In addition to the steric component, the higher stabilization of the cit-Fe_3O_4 particles when comparing to bare ones could also be attributed to the higher

Table 1
Hydrodynamic size (D_H), polydispersity index (PdI) and zeta potential (ζ) of the multiple obtained particles.

	D_H (nm)	PdI	ζ (mV)
Fe_3O_4	68 ± 20	0.3 ± 0.01	34.6 ± 0.1
Cit-Fe_3O_4	42 ± 15	0.38 ± 0.02	−44.5 ± 0.6
CS	325 ± 68	0.21 ± 0.01	28.4 ± 0.7
Cit-Fe_3O_4/CS	339 ± 66	0.19 ± 0.01	24.6 ± 0.9
Lyophilized cit-Fe_3O_4/CS	483 ± 8	0.31 ± 0.02	19.1 ± 0.1
Lyophilized cit-Fe_3O_4/CS + 5 % saccharose	377 ± 49	0.13 ± 0.01	25.6 ± 0.5
Lyophilized cit-Fe_3O_4/CS + 5 % saccharose after saccharose removal	368 ± 72	0.19 ± 0.01	23.7 ± 0.9

hydrophilicity observed for cit-Fe_3O_4 in the performed contact angle analysis (see section *3.1.3. Surface thermodynamics*) compared to bare Fe_3O_4 particles [20].

CS NPs and cit-Fe_3O_4/CS NPs showed similar hydrodynamic size and ζ values. Therefore, CS coacervation methodology does not suffer significative changes when cit-Fe_3O_4 are included. In addition, it was determined that the yield of the cit-Fe_3O_4/CS NPs production was 56.8 ± 4 %. Therefore, the magnetic isolation and yield obtaining to produce cit-Fe_3O_4/CS can explain the differences observed between the proportions used in the preparation procedure and the results obtained from TGA (see section *3.1.2.*).

The DLS analysis of the dispersed cit-Fe_3O_4/CS particle size in water at initial time and after 1 week was 332.76 ± 84.07 and 343.71 ± 88.05 nm, respectively. In PBS, the DLS values obtained for cit-Fe_3O_4/CS NPs were 333.53 ± 74.05 and 363.73 ± 66.06 nm for the initial time and after 1 week, respectively. Therefore, the calculated colloidal stability using equation (2), was 1.03 in water and 1.09 in PBS, which falls within the acceptable range of 1–1.5 according to the literature [29,43]. ZP values were used to assess the CS coating stability of the cit-Fe_3O_4/CS nanoparticles. The values obtained for ζ of the cit-Fe_3O_4/CS NPs in water were 26.62 ± 0.17 and 27.5 ± 0.47 mV, for the initial time and after 1 week, respectively. In PBS, the values obtained for ζ of the cit-Fe_3O_4/CS NPs were 22.1 ± 0.92 and 21.9 ± 0.25 mV. Therefore, the results of short-time colloidal stability results for cit-Fe_3O_4/CS NPs demonstrated the adequate properties of CS in maintaining particles stability in both aqueous and PBS. This is in line with previous investigations [22].

The long-term storage of NP suspensions possesses an increased risk of the most common instability problems (i.e., particle aggregation, hydrolysis, or microbiological contamination). Thus, to protect the cit-Fe_3O_4/CS NPs size and stability, water removal appears as the most effective approach, being freeze-drying probably the most used process in biopharmaceutical field. With that aim, specific excipient can be used as they can provide sufficient lyoprotection [44,45]. In this research, freeze-drying of cit-Fe_3O_4/CS NPs was performed in the absence and in the presence of saccharose (5 %, w/v). When reconstituted, lyophilized cit-Fe_3O_4/CS NPs without saccharose showed an increase in the hydrodynamic size of the particles, a broader PdI, and a moderate decrease in the surface electrical charge in terms of ζ, when compared with non-lyophilized cit-Fe_3O_4/CS NPs (Table 1). These undesirable modification of the cit-Fe_3O_4/CS NPs could be attributed to inter and intramolecular hydrogen bounding of surface located CS [46]. However, negligible changes were obtained when performing the freeze-drying procedure of the cit-Fe_3O_4/CS NPs in presence of 5 % w/v saccharose, both before and after saccharose removal by magnetic isolation. This finding is consistent with previous reports on CS-based nanoformulations [44,45]. This excipient probably creates a glassy matrix embedding the NPs. Thus, saccharose could protect NPs from aggregation and mechanical stress of ice crystals [46].

HRTEM analysis demonstrated a particle size of 12 ± 3.86 nm and low PdI of the cit-Fe_3O_4 (Fig. 2a), demonstrating that cit functionalization did not affect the size of this magnetic colloids compared to bare Fe_3O_4 obtained by the same synthesis method reported by some of us [33]. Thus, the resultant particles exhibited appropriate characteristic for engineering hyperthermia agents [11,47]. The size obtained for cit-Fe_3O_4 NPs by DLS (Table 1) was greater than that obtained by HRTEM (Fig. 2a), as is frequently observed. The surface of the particles possesses strong electrostatic repulsion forces, inducing a higher hydrodynamic size and, therefore, a higher value of size by the DLS technique [42]. Cluster of nuclei embedded into a polymeric nanomatrix were observed in Fig. 2b with a size of 187.33 ± 54.85 nm. Furthermore, the particles in Fig. 2c were very similar to those of Fig. 2b which confirms the preservation of cit-Fe_3O_4/CS nanostructure after the freeze-drying procedure when saccharose was used. In addition, size determination of freeze-dried cit-Fe_3O_4/CS particles was very similar to that obtained for cit-Fe_3O_4/CS ones (176.51 ± 63.39 and 187.33 ± 54.85 nm, respectively).

Electrophoretic light scattering technique was used for the electrophoresis of Fe_3O_4, cit-Fe_3O_4, CS and cit-Fe_3O_4/CS NPs as a function of pH and ionic strength (Fig. 3). At a fixed ionic strength ($KNO_3 = 10^{-3}$ M), the ζ values were determined as a function of the pH (fixed with HNO_3 and KOH). When Fe_3O_4 was functionalized with cit (cit-Fe_3O_4), isoelectric point shifted from pH 7 [48] to pH 3 (Fig. 3a). In addition, negative ζ values were obtained for the whole pH range (Fig. 3a), probably due to the deprotonation of the two carboxylic groups of cit-Fe_3O_4 [40]. On the contrary, in the CS NPs and when cit-Fe_3O_4 particle cluster are embedded in the CS nanomatrix, positive values appeared in the whole pH range studied (Fig. 3a), which may be due to the protonation of the residual amino groups presented in the CS structure [22]. In contrast of the electrokinetic behaviour of Fe_3O_4 under different pH media, negligible dependence was found when varying the ionic strength media (Fig. 3b), as previously reported [48]. Such tendence was also showed by the rest of the NPs investigated (Fig. 3b). Thus, differences and similarities were confirmed between the Fe_3O_4 and cit- Fe_3O_4 and cit-Fe_3O_4/CS and CS NPs, respectively. Hence, both efficient surface functionalization of Fe_3O_4 with cit and coating of the cit-Fe_3O_4 particles by CS could be postulated.

3.1.2. Thermogravimetric, Fourier transform infrared and X-ray diffractometry analysis

TGA of Fe_3O_4 and cit-Fe_3O_4/CS NPs were used to study the thermal stability and decomposition pattern (Fig. 4). Results were in agreement with previously reported investigations [13,49,50].

The obtained thermogram for cit-Fe_3O_4/CS NPs presented two stage weight (wt) loss patterns. First, a total degradation of 33.12 wt % occurs below 600 °C, which corresponds to evaporation of surface adsorbed moisture (7.32 wt %), the cit used for the Fe_3O_4 colloids functionalization (9.24 wt %) and the CS matrix of the cluster/shell NPs (16.56 wt %). Then, the wt loss curve shows a total degradation of 66.88 % wt up to 800 °C, which has been associated to Fe_3O_4 reduction to hematite or maghemite. In addition to determine their Fe_3O_4 wt ratio, the thermogram demonstrated that Fe_3O_4, cit and CS are present in the cit-Fe_3O_4/CS NPs, as their degradation occurs in their characteristic temperatures. Concretely, these are 233 °C and 362 °C for cit and CS, respectively, and 685 and 790 °C for Fe_3O_4 colloids. The Fe_3O_4 and cit-Fe_3O_4/CS slight weight gain above 300 and 650 °C, could be ascribed to partial oxidation of magnetite to hematite or maghemite [13]. Although a N_2 atmosphere 99.9 % pure was used during the experiment, a small amount of O_2, together with the potential air entrapped between the powder particles during the preparation of the sample, can explain some degree of oxidation of the magnetic particles. The high concentration of Fe^{2+} and the relatively small mass gain suggests in any case that the amount of oxygen must be very low, and it should not lead to any significant

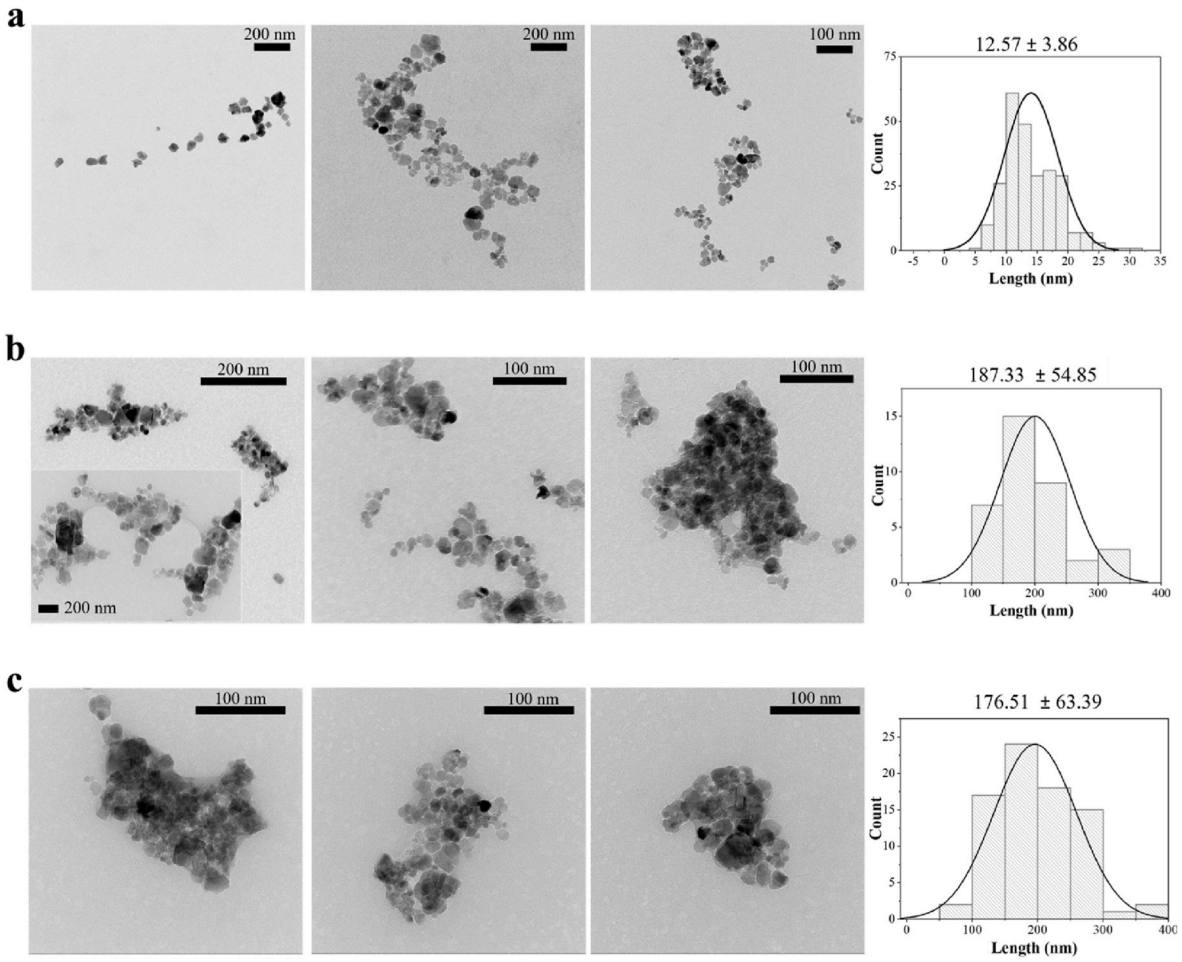

Fig. 2. HRTEM and particle size distribution of the (*a*) cit-Fe_3O_4, (*b*) cit-Fe_3O_4/CS, and (*c*) lyophilized cit-Fe_3O_4/CS NPs in the presence of 5 % w/v saccharose particles.

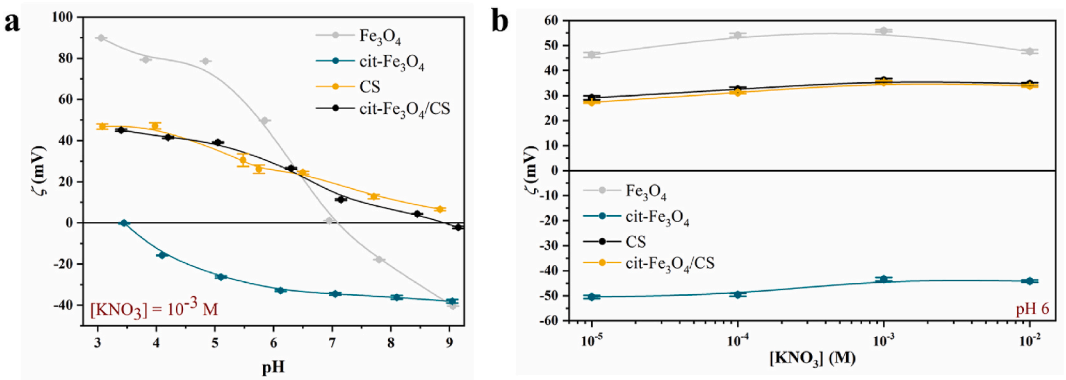

Fig. 3. Zeta potential (ζ, mV) of the Fe_3O_4 (○), cit-Fe_3O_4 (●), CS (□) and cit-Fe_3O_4/CS (■) particles as a function of (*a*) pH at a fixed [KNO_3] = 10^{-3} M and (*b*) the KNO_3 molar concentration at pH 6.

mistake in the interpretation of the TGA data.

The resultant cit-Fe_3O_4 and cit-Fe_3O_4/CS NPs were characterized by FTIR. Pure Fe_3O_4 and CS NPs spectrum were used as controls. The IR absorption spectra (Fig. 5a) were consistent with the already reported data [32,50–52]. The broad bands identified around 3400 cm^{-1} may be associated to O–H stretch and bond present in the Fe_3O_4 and cit-Fe_3O_4 particles surface. In this region can also be found the N–H stretch peak in the CS NPs spectra. Because of the more polar nature of O–H, the stretching vibration of this group is expected to be more intense than the one from N–H stretching, thus it is the main one appearing in the cit-Fe_3O_4/CS NPs spectra. The C–H stretch peaks can be found between 2850 and 3300 cm^{-1}, depending on the hybridization. This peak has been shown in the cit-Fe_3O_4 spectra, but not in the one of the bare Fe_3O_4. Therefore, the efficacy of the cit-functionalization procedure of the Fe_3O_4 could be confirm. Furthermore, two C–H stretch peaks could be identified in both CS NPs and cit-Fe_3O_4/CS NPs spectrum. As CS polysaccharide is the product of chitin deacetylation process, C═O stretching from amide groups can be identified at 1630 cm^{-1} in CS NPs and

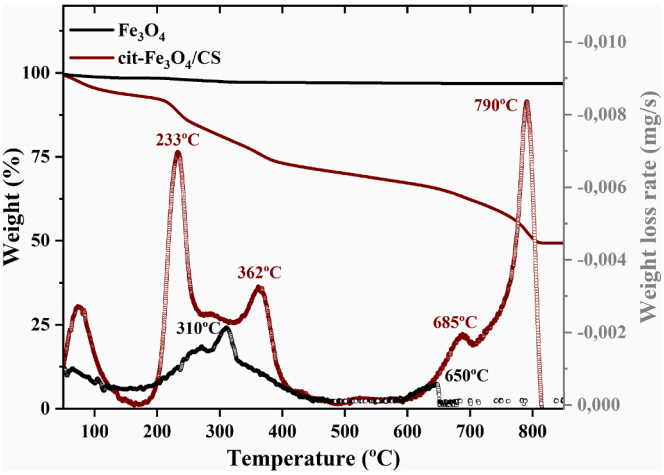

Fig. 4. Thermogram of the Fe_3O_4 and cit-Fe_3O_4/CS NPs in terms of weight (%) and weight loss rate (mg/s).

cit-Fe_3O_4/CS NPs analysis. The absorption bands of low intensities in the region of 550 cm^{-1} are attributed to the stretching vibrations of metal oxide (Fe–O) bonds. Then, they are present in pure Fe_3O_4, in cit-Fe_3O_4, and in cit-Fe_3O_4/CS NPs (Fig. 5a).

Fig. 5b presents the XRD pattern for cit-Fe_3O_4/CS. For comparison purposes, Fig. 5c depicts the Fe_3O_4 pattern reported by the American Society for Testing and Materials. The results indicated the mineralogical purity and high crystalline nature of the synthesized Fe_3O_4, even after its modification with cit and CS.

3.1.3. Surface thermodynamics

The analysis of the surface thermodynamics of NPs is of high utility to confirm the engineering of cit-Fe_3O_4 and cit-Fe_3O_4/CS NPs. The surface thermodynamics analysis of the NPs began by measuring the θ of three liquids on the dry NPs layers. The findings indicated notable distinctions among the three NPs studied (Fig. 6a). However, a more comprehensive characterization of the particle surface thermodynamics was obtained by determining the surface energy (γ_S), as shown in Fig. 6b. The free energy of interaction (ΔG_{SLS}) between the solids and the liquid was evaluated to determine the hydrophilic or hydrophobic colloids nature. A negative value of ΔG_{SLS} indicates a hydrophobic character where interfacial interactions favor attraction between the NPs. In contrast, a positive value of ΔG_{SLS} is associated with hydrophilic behaviour. A more positive ΔG_{SLS} value was obtained for cit-Fe_3O_4 NPs than those previous found for bare Fe_3O_4 colloids [20]. On the contrary, a negative ΔG_{SLS} value resulted for CS particles probably due to its amphiphilic nature [14]. During the drying process of the CS sample, it is likely that more hydrophobic groups were oriented towards the outer layer, resulting in a hydrophobic surface. Such behaviour is in accordance with previous literature [33]. As expected, similar surface thermodynamics results were found for CS and cit-Fe_3O_4/CS NPs, indicating that the CS shell completely covers the cit-Fe_3O_4 particles cluster.

3.1.4. Magnetic characterization

Magnetic characterization results of cit-Fe_3O_4 and cit-Fe_3O_4/CS NPs are depicted in Fig. 7. The cit-Fe_3O_4 and cit-Fe_3O_4/CS NPs displayed a very similar magnetic behaviour, and maximum magnetization (M_{max}) values of 84.5 ± 3.7 and 85.2 ± 1.6 emu/g for cit-Fe_3O_4 and cit-Fe_3O_4/CS NPs, respectively. These results showed a promising magnetic character when comparing with other Fe_3O_4-based NPs [12], as they are very close to those described for bulk Fe_3O_4 value (92 emu/g) [53]. In fact, these data showed remarkable magnetic properties taking into account that CS modified Fe_3O_4 colloids previously reported usually showing around 60 emu/g values [16].

The suitable magnetic responsive behaviour of the cit-Fe_3O_4 and cit-

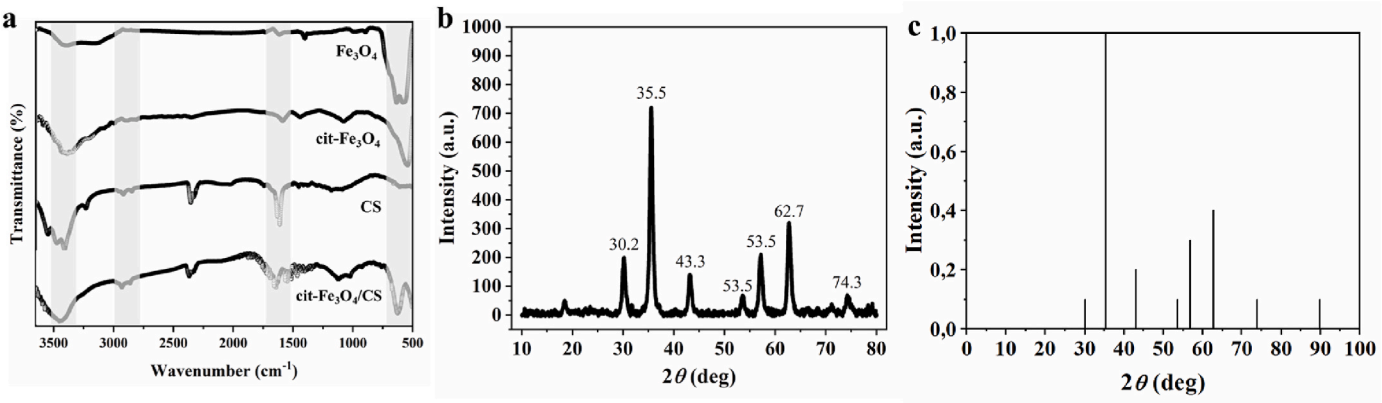

Fig. 5. FTIR spectrum of Fe_3O_4, cit-Fe_3O_4, CS and cit-Fe_3O_4/CS NPs. The grey shadow highlights the most significant peaks for the analysis (*a*). X-ray diffractograms of cit-Fe_3O_4/CS NPs (*b*) and American Society for Testing and Materials (ASTM) pattern for Fe_3O_4 (*c*). The intensity is expressed in arbitrary units (a. u.).

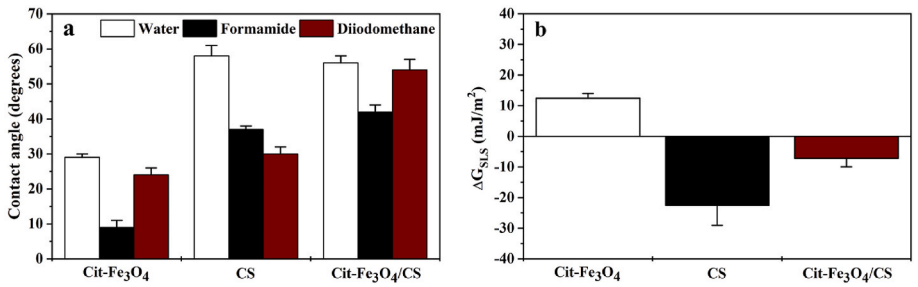

Fig. 6. Contact angle (θ, degrees) of water, formamide, and diiodomethane on cit-Fe_3O_4, CS, and cit-Fe_3O_4/CS NPs layers (*a*). (c) ΔG_{SLS} (solid–liquid interfacial energy of interaction) values (mJm^{-2}) and hydrophobic/hydrophilic character of the three types of NPs.

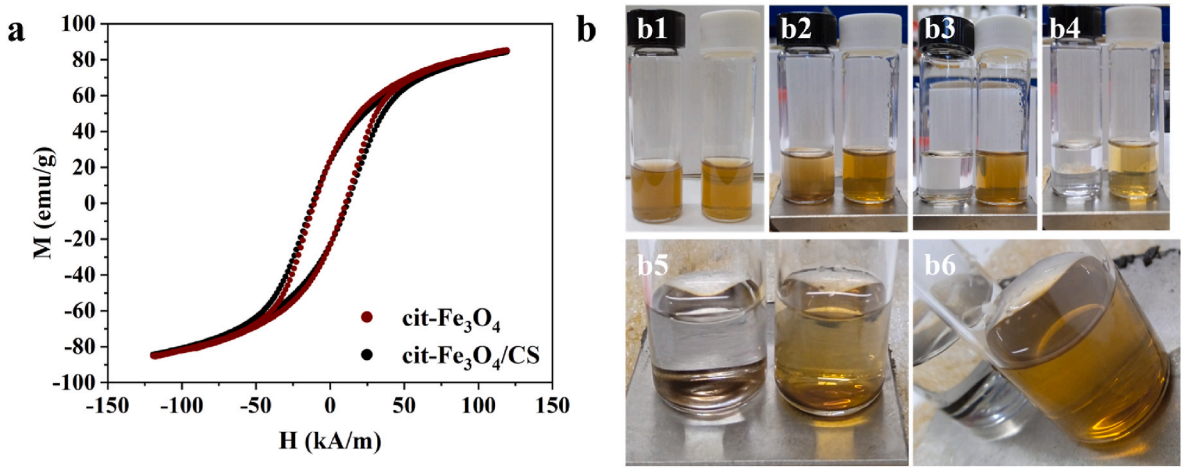

Fig. 7. Magnetization cycle of the cit-Fe_3O_4 and cit-Fe_3O_4/CS NPs at a frequency of 1.5 kHz. Visual observation of an aqueous dispersion (0.5 %, w/v) of cit-Fe_3O_4/CS NPs (left) and cit-Fe_3O_4 (right) without a permanent magnet (b1), and with a permanent magnet at sequential time points of 5 s (b2), 1 min (b3), and 1 h (b4-b6).

Fe_3O_4/CS NPs is further illustrated in Fig. 7b. Complete magnetic attraction of the cit-Fe_3O_4/CS NPs towards the magnet occurred within 1 min, whereas only partial attraction was observed for cit-Fe_3O_4 NPs throughout the entire experiment. This could be explained by the enhanced magnetic character of cit-Fe_3O_4 when they are included as a cluster of particles within the CS shell, comparing when they are single-core particles. Thus, this preliminary test demonstrated the potential of cit-Fe_3O_4/CS NPs to be magnetically guided to the tumor.

3.2. Magnetic hyperthermia and photothermal characterization

Experiment conditions were carefully selected regarding clinical safety limits for MH and PT. For MH, frequency and magnetic field strength of the AMF met the criteria for tolerable limits ($H \times f = 4.85 \times 10^8$ $Am^{-1}s^{-1}$–9.59×10^9 $Am^{-1}s^{-1}$) [54], while for PT, a wavelength in the first biological transparency window (NIR-I) was chosen in addition of laser power densities within the range of acceptable values previously described [55]. Therefore, our research was focused on evaluating the impact of heating induced by NPs at mild conditions where the impact of tissue damage caused solely by the AMF, or the laser power irradiation would be negligible.

For MHT, a frequency sweep (120–190 kHz) was performed in a moderate AMF condition of 16 kA/m (Table 2). Given the SAR and ΔT (°C) results (Table 2), 120 kHz was the selected as the optimal frequency for both NPs.

The data depicted in Table 2 showed that cit-Fe_3O_4 exhibits heating capacity, as evidence by ΔT values, sufficient to reach, at the very least, the minimum temperature required for antitumor hyperthermia in physiological conditions (ΔT > 6 °C) [56] in all the tested conditions. The size of the cit-Fe_3O_4 NPs (15 ± nm) found in HRTEM, contributes to the colloidal stability, as no attractive interactions between the particles would occur due to the remanent magnetic moments typical of ferromagnetic particles [57]. As expected, the thermal efficiency decreases slightly for coated particles cit-Fe_3O_4/CS NPs as compared to cit-Fe_3O_4 NPs, due to the presence of the CS as a magnetically inert polymer, for the same concentration of nanoparticles. Nevertheless, the opposite arises when comparing maximum SAR values: cit-Fe_3O_4 exhibited lower values than cit-Fe_3O_4/CS NPs. SAR values for cit-Fe_3O_4 NPs were in line with previous reported values for similar colloids [12]. SAR values had been reported to be independent of concentration, excluding certain cases (i.e. high concentration or particles aggregation) [58,59]. Thus, cit-Fe_3O_4/CS NPs could display higher SAR values than cit-Fe_3O_4, probably due to magnetic interactions between the multiple cit-Fe_3O_4 particles when forming a cluster that constitute cit-Fe_3O_4/CS NPs, as it has been recently reported [60]. Indeed, the higher SAR values achieved for cit-Fe_3O_4/CS NPs were superior to that obtained for single core/shell particles [16,17]. Therefore, the cluster/shell strategy holds promise in enhancing SAR values.

In PTT, cit-Fe_3O_4 and cit-Fe_3O_4/CS NPs displayed ΔT values appropriate for hyperthermia therapy (Table 3) [56]. For both NPs SAR values depend on laser power irradiation increasing with laser power irradiation (Table 3). The potential of the cit-Fe_3O_4 and cit-Fe_3O_4/CS developed in PTT is noteworthy. When comparing SAR values for the two types of NPs, SAR values were always greater for cit-Fe_3O_4/CS NPs. In this regard, it is worth emphasizing that previous studies have shown that formation of magnetic NPs clusters can result in a shift towards longer wavelengths in the absorption spectrum of light, leading to an increased absorption rate in the NIR region. That phenomenon had been broadly investigated for gold NPs clusters. Recently, very few papers have been reported for the application of Fe_3O_4 NPs clusters for NIR irradiation [61,62], and none of them uses CS polymer for obtaining such nanostructure. As pure CS NPs display no absorption at the NIR wavelength used for the experiments [63], it may act as an adjuvant for heating efficiency of Fe_3O_4 in PT by favouring low decreasing interparticle distances of cit-Fe_3O_4 colloids thanks to the stable nanomatrix formed around them (Fig. 2b and c). Thus, the use of cit-Fe_3O_4/CS NPs may be a promising alternative for PT antitumor therapy with a more

Table 2
SAR (W/g) and ΔT (°C) values of cit-Fe_3O_4 and cit-Fe_3O_4/CS NPs in terms of frequency at a fixed amplitude and concentration of 16 kA/m and 5 mg/mL, respectively.

Sample	Frequency (kHz)	SAR (W/g)	ΔT(°C)
Cit-Fe_3O_4 NPs	120	239 ± 31	32.5 ± 0.2
	140	188 ± 30	16.2 ± 0.2
	190	167 ± 40	15.0 ± 0.2
Cit-Fe_3O_4/CS NPs	120	393 ± 45	9.2 ± 0.2
	140	181 ± 26	8.6 ± 0.2
	190	93 ± 11	6.3 ± 0.2

Table 3
SAR (W/g) and ΔT (°C) values of cit-Fe_3O_4 and cit-Fe_3O_4/CS NPs in terms of laser power density at 5 mg/mL NPs, respectively.

Power density (W/cm^2)	cit-Fe_3O_4			cit-Fe_3O_4/CS		
	SAR (W/g)	Error	ΔT (°C)	SAR (W/g)	Error	ΔT (°C)
1	69.1	0.3	3.7	184.1	1.5	6.4
1.5	265.4	1.0	7.2	337.0	2.0	8.8
2	272.0	0.8	17.3	384.0	7.1	11.2

biocompatible profile when comparing to the current strategies (i.e. use of high concentration of Fe_3O_4 NPs or combination with organic dyes) [64].

When comparing the MHT and PTT hyperthermia modalities for the developed cit-Fe_3O_4/CS NPs, similar efficiencies in terms of SAR values were found (Fig. 8). In MHT, colloidal stability plays an essential role in the heating efficiency [54]. In PTT, the distance between particles seems to be an important factor contributing to the heating enhancement [61, 62]. Taken together, the cluster/shell cit-Fe_3O_4/CS NPs proved to be promising agents for MHT and PTT, and future research will reveal whether the simultaneous application of both modalities could imply a synergistic effect, making the biomedical use of cluster/shell cit-Fe_3O_4/CS NPs even more feasible.

3.3. Citotoxicity and haemocompatibility

Negligible cytotoxicity was observed with cit-Fe_3O_4/CS NPs in BV2 cells, as no statistically significant differences in cell growth were detected between the control group and cells incubated with cit-Fe_3O_4/CS NPs at any of the investigated concentrations (Fig. 9).

NPs may provoke interaction with blood components when administered by a systemic administration route, leading to adverse effects of the NP-based treatment (e.g. thrombotic complications, anaphylaxis, renal damage, or anemia) [31,37]. Therefore, for biomedical applications, it is essential to perform an haemocompatibility assay. Data from blood compatibility assay of cit-Fe_3O_4/C NPs is compiled in Table 4. Negligible effects were found on erythrocytes (haemolysis), platelet and complement system activation, a plasma clotting time, in accordance with previous magnetic/polymeric NPs [15]. Then, these NPs could be used for systemic administration route. This research also served to preliminary confirm biocompatibility of cit-Fe_3O_4/CS. Future *in vivo* experiments will be necessary to define safety margin of these NPs.

4. Conclusions

In this study, we have designed and synthesized efficient Fe_3O_4 colloids (15 ± nm) by chemical co-precipitation methodology. Resulted bare Fe_3O_4 colloids were functionalized with cit to provide steric repulsions and a highly hydrophilic surface to the NPs. The developed cit-Fe_3O_4 particles clustered inside a CS-based nanomatrix by a coacervation procedure were found to be a very promising approach to optimized heating efficiency of cit-Fe_3O_4 colloids for the biomedical application of antitumor hyperthermia therapy. CS demonstrated to be an outstanding material to completely coat multiple cit-Fe_3O_4, and thus obtaining a cluster/shell NPs showing appropriate characteristic such as 339 ± 66 nm, a potential steric stabilization, and a preliminar biocompatible profile based on negligible effects on BV2 cell line and a haemocompatible profile. Furthermore, long-term stability of the cit-Fe_3O_4/CS NPs was demonstrated by freeze-drying using saccharose as cryoprotectant.

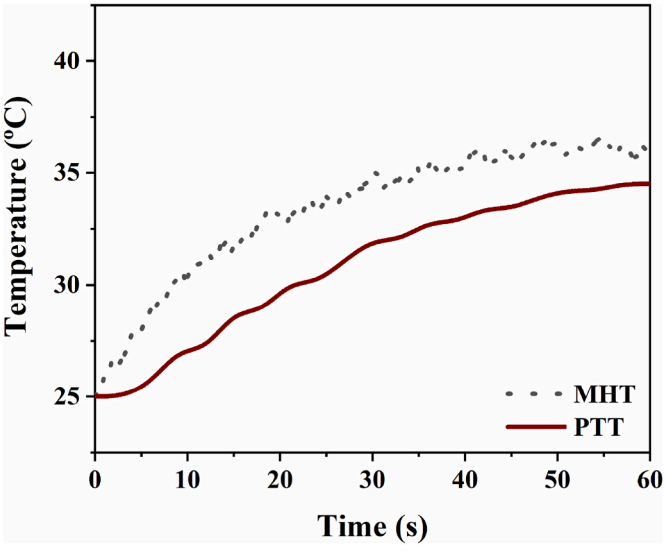

Fig. 8. Temperature increases for cit-Fe_3O_4/CS NPs (5 mg/ml) in MHT (120 kHz and 16 kA/m) and PTT (850 nm and 2 W/cm^2) modalities.

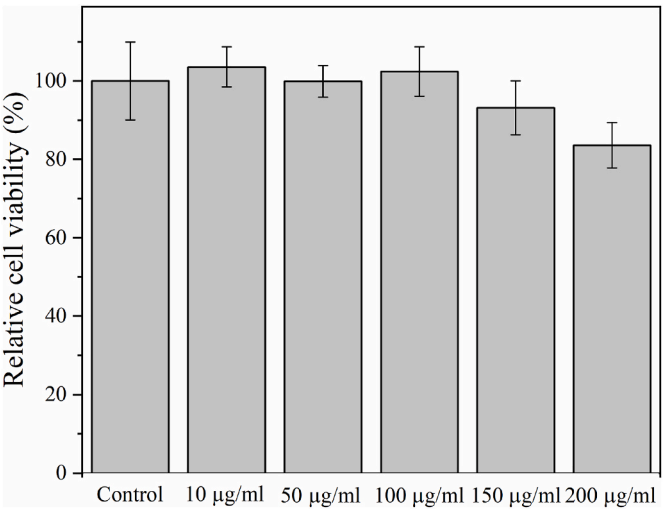

Fig. 9. *In vitro* cytotoxicity of the cit-Fe_3O_4/CS NPs in BV2 microglia cells. Cell lines were kept in contact with the particles for 24 h. Data are presented as mean values and error bars denote the SEM of at least three independent experiments performed in triplicate.

In addition, we provide a comprehensive comparison of the heating efficiency of cit-Fe_3O_4 as single core and cit-Fe_3O_4 as cluster (cit-Fe_3O_4/CS NPs) under experimental conditions of varying AMF frequency and laser power density. These experiments confirm that cit-Fe_3O_4 NPs were highly efficient for MHT and for PTT in all tested scenarios.

More interestingly, when considering SAR values, cit-Fe_3O_4/CS NPs were found to be more efficient than cit-Fe_3O_4 NPs under all the tested conditions in PTT, and for nearly all conditions in MHT. Thus, we demonstrated that cluster cit-Fe_3O_4 behaviour is an effective strategy to design Fe_3O_4-based hyperthermia agents. To the best of our knowledge, this is the first time that CS has demonstrated to behave as a promising adjuvant for hyperthermia enhancing heating efficiency when creating a Fe_3O_4-based cluster/shell structure.

In summary, these cit-Fe_3O_4/CS NPs cluster/shell NPs may constitute a potential candidate for a systemic administered dual magneto-photothermal therapeutic against cancer. Future experiments will disclose the antitumor efficacy and potential synergistic effect when using this strategy.

CRediT authorship contribution statement

Gracia García-García: Writing – review & editing, Writing – original draft, Validation, Methodology, Investigation, Formal analysis, Data curation, Conceptualization. **Marina Lázaro:** Writing – review & editing, Writing – original draft, Validation, Formal analysis. **Alejandro Cenalmor:** Validation, Formal analysis. **Isabel García-Álvarez:** Resources, Funding acquisition, Validation, Formal analysis, Supervision. **Guillermo R. Iglesias:** Writing – review & editing, Supervision, Resources, Funding acquisition, Conceptualization. **José L. Arias:** Writing – review & editing, Writing – original draft, Supervision, Resources, Funding acquisition, Conceptualization.

Declaration of competing interest

The authors declare that they have no known competing financial

Table 4
Blood compatibility of the cit-Fe_3O_4/CS cluster/shell particles: haemolysis (%), platelet activation (sP-selectin release, ng/mL), complement activation (C3a release: C3a desArg, ng/mL), and plasma recalcification time ($T_{1/2}$ max, min).

Sample	Haemolysis (%)				sP-selectin release (ng/mL)	C3a desArg (ng/mL)	$T_{1/2max}$ (min)
	Incubation time						
	2 h	4 h	8 h	24 h			
cit-Fe_3O_4/CS	2.3 ± 0.6	2.2 ± 0.5	2.5 ± 0.6	2.4 ± 0.3	105 ± 6	303 ± 7	13.3 ± 1.5
Control (PBS)	0	0	0	0	101 ± 4	295 ± 7	11.6 ± 1.3

interests or personal relationships that could have appeared to influence the work reported in this paper.

Acknowledgements

This work was supported by Universidad Francisco de Vitoria (UFV2022-11). FEDER/Junta de Andalucía-Consejería de Transformación Económica, Industria, Conocimiento y Universidades, Spain (Grant No. P20_00346) and Consejería de Conocimiento, Investigación y Universidad, Junta de Andalucía, 595 Spain (Grant No, A-FQM492-UGR20) is gratefully acknowledged. G.R.I, M.L, thanks are also due for the grant TED2021-131855BI00/AEI/10.13039/501100011033/Unión Europea Next Generation EU/PRTR. European Union's Horizon 2020 research and innovation programme under the Marie Sklodowska-Curie grant agreement No 10106426.

References

[1] D. Jaque, L. Martínez Maestro, B. del Rosal, P. Haro-Gonzalez, A. Benayas, J. L. Plaza, E. Martín Rodríguez, J. García Solé, Nanoparticles for photothermal therapies, Nanoscale 6 (2014) 9494–9530, https://doi.org/10.1039/c4nr00708e.
[2] C. De-Colle, A. Beller, C. Gani, N. Weidner, V. Heinrich, U. Lamprecht, S. Gaupp, O. Voigt, O. Dohm, D. Zips, A.C. Müller, Radiotherapy and hyperthermia for breast cancer patients at high risk of recurrence, Int. J. Hyperther. 39 (2022) 1010–1016, https://doi.org/10.1080/02656736.2022.2103593.
[3] Y.J. Hou, X.X. Yang, R.Q. Liu, D. Zhao, C.X. Guo, A.C. Zhu, M.N. Wen, Z. Liu, G. F. Qu, H.X. Meng, Pathological mechanism of photodynamic therapy and photothermal therapy based on nanoparticles, Int. J. Nanomed. 15 (2020) 6827–6838, https://doi.org/10.2147/IJN.S269321.
[4] Q. Yu, X. Tang, W. Zhao, Y. Qiu, J. He, D. Wan, J. Li, X. Wang, X. He, Y. Liu, M. Li, Z. Zhang, Q. He, Mild hyperthermia promotes immune checkpoint blockade-based immunotherapy against metastatic pancreatic cancer using size-adjustable nanoparticles, Acta Biomater. 133 (2021) 244–256, https://doi.org/10.1016/j.actbio.2021.05.002.
[5] A.A. Petryk, A.J. Giustini, R.E. Gottesman, P.A. Kaufman, P.J. Hoopes, Magnetic nanoparticle hyperthermia enhancement of cisplatin chemotherapy cancer treatment, Int. J. Hyperther. 29 (2013) 845–851, https://doi.org/10.3109/02656736.2013.825014.
[6] E. Boisselier, D. Astruc, Gold nanoparticles in nanomedicine: preparations, imaging, diagnostics, therapies and toxicity, Chem. Soc. Rev. 38 (2009) 1759–1782, https://doi.org/10.1039/b806051g.
[7] C. Blanco-Andujar, F.J. Teran, D. Ortega, Current outlook and perspectives on nanoparticle-mediated magnetic hyperthermia, in: M. Mahmoudi, S. Laurent (Eds.), Iron Oxide Nanoparticles for Biomedical Applications, Elsevier Ltd, 2018, pp. 197–245, https://doi.org/10.1016/B978-0-08-101925-2.00007-3.
[8] I. Hilger, In vivo applications of magnetic nanoparticle hyperthermia, Int. J. Hyperther. 29 (2013) 828–834, https://doi.org/10.3109/02656736.2013.832815.
[9] T.J. Yu, P.H. Li, T.W. Tseng, Y.C. Chen, Multifunctional Fe_3O_4/alumina core/shell MNPs as photothermal agents for targeted hyperthermia of nosocomial and antibiotic-resistant bacteria, Nanomedicine 6 (2011) 1353–1363, https://doi.org/10.2217/nnm.11.34.
[10] M.Y. Liao, P.S. Lai, H.P. Yu, H.P. Lin, C.C. Huang, Innovative ligand-assisted synthesis of NIR-activated iron oxide for cancer theranostics, Chem comm 48 (2012) 5319–5321, https://doi.org/10.1039/c2cc31448g.
[11] M. Chu, Y. Shao, J. Peng, X. Dai, H. Li, Q. Wu, D. Shi, Near-infrared laser light mediated cancer therapy by photothermal effect of Fe3O4 magnetic nanoparticles, Biomaterials 34 (2013) 4078–4088, https://doi.org/10.1016/j.biomaterials.2013.01.086.
[12] A. Espinosa, R. Di Corato, J. Kolosnjaj-Tabi, P. Flaud, T. Pellegrino, C. Wilhelm, Duality of iron oxide nanoparticles in cancer therapy: amplification of heating efficiency by magnetic hyperthermia and photothermal bimodal treatment, ACS Nano 10 (2016) 2436–2446, https://doi.org/10.1021/acsnano.5b07249.
[13] M. Lázaro, P. Lupiáñez, J.L. Arias, M.P. Carrasco-Jiménez, Á.V. Delgado, G. R. Iglesias, Combined magnetic hyperthermia and photothermia with polyelectrolyte/gold-coated magnetic nanorods, Polymers 14 (2022) 4913, https://doi.org/10.3390/polym14224913.
[14] H. Hamedi, S. Moradi, S.M. Hudson, A.E. Tonelli, M.W. King, Chitosan based bioadhesives for biomedical applications: a review, Carbohydr. Polym. 282 (2022) 119100, https://doi.org/10.1016/j.carbpol.2022.119100.
[15] F. Fernández-Álvarez, C. Caro, G. García-García, M.L. García-Martín, J.L. Arias, Engineering of stealth (maghemite/PLGA)/chitosan (core/shell)/shell nanocomposites with potential applications for combined MRI and hyperthermia against cancer, J. Mater. Chem. B 9 (2021) 4963–4980, https://doi.org/10.1039/d1tb00354b.
[16] P.B. Shete, R.M. Patil, N.D. Thorat, A. Prasad, R.S. Ningthoujam, S.J. Ghosh, S. H. Pawar, Magnetic chitosan nanocomposite for hyperthermia therapy application: preparation, characterization and in vitro experiments, Appl. Surf. Sci. 288 (2014) 149–157, https://doi.org/10.1016/j.apsusc.2013.09.169.
[17] P.I. Soares, D. Machado, C. Laia, L.C. Pereira, J.T. Coutinho, I.M. Ferreira, C. M. Novo, J.P. Borges, Thermal and magnetic properties of chitosan-iron oxide nanoparticles, Carbohydr. Polym. 149 (2016) 382–390, https://doi.org/10.1016/j.carbpol.2016.04.123.
[18] Y. Zheng, W. Wang, J. Zhao, C. Wu, C. Ye, M. Huang, S. Wang, Preparation of injectable temperature-sensitive chitosan-based hydrogel for combined hyperthermia and chemotherapy of colon cancer, Carbohydr. Polym. 222 (2019) 115039, https://doi.org/10.1016/j.carbpol.2019.115039.
[19] G. García-García, M. Lázaro-Callejón, F. Fernández-Álvarez, G.R. Iglesias, J. L. Arias, Magnetite/poly(ε-caprolactone))/chitosan (core/shell)/shell nanocomposites with potential applications in hyperthermia cancer therapy, J. Magn. Magn Mater. 588 (2023) 171500, https://doi.org/10.1016/j.jmmm.2023.171500. - 171500.
[20] G. García-García, F. Fernández-Álvarez, L.Á.V. Cabeza, Delgado, C. Melguizo, J. C. Prados, J.L. Arias, Gemcitabine-loaded magnetically responsive poly (ε-caprolactone) nanoparticles against breast cancer, Polymers 12 (2020) 2790, https://doi.org/10.3390/polym12122790.
[21] G. García-García, C. Caro, F. Fernández-Álvarez, M.L. García-Martín, J.L. Arias, Multi-stimuli-responsive chitosan-functionalized magnetite/poly (ε-caprolactone) nanoparticles as theranostic platforms for combined tumor magnetic resonance imaging and chemotherapy, Nanomedicine: NBM. (2023) 102695, https://doi.org/10.1016/j.nano.2023.102695.
[22] F. Fernández-Álvarez, G. García-García, J.L. Arias, A tri-stimuli responsive (maghemite/PLGA)/chitosan nanostructure with promising applications in lung cancer, Pharmaceutics 13 (8) (2021) 1232, https://doi.org/10.3390/pharmaceutics13081232.
[23] F. Fernández-Álvarez, G. García-García, G.R. Iglesias, J.L. Arias, A maghemite/PLGA (core/shell) nanostructure that may facilitate chemotherapy and antitumor hyperthermia, J. Magn. Magn Mater. 589 (2024) 171574, https://doi.org/10.1016/j.jmmm.2023.171574.
[24] V. Hsieh, S. Okada, H. Wei, I. García-Álvarez, A. Barandov, S.R. Alvarado, R. Ohlendorf, J. Fan, A. Ortega, A. Jasanoff, Neurotransmitter-responsive nanosensors for T2-weighted magnetic resonance imaging, J. Am. Chem. Soc. 141 (2019) 15751–15754, https://doi.org/10.1021/jacs.9b08744.
[25] H.A. Albarqi, L.H. Wong, C. Schumann, F.Y. Sabei, T. Korzun, X. Li, M.N. Hansen, P. Dhagat, A.S. Moses, O. Taratula, Biocompatible nanoclusters with high heating efficiency for systemically delivered magnetic hyperthermia, ACS Nano 13 (2019) 6383–6395, https://doi.org/10.1021/acsnano.8b06542.
[26] Y. Wang, X. Li, P. Chen, Y. Dong, G. Liang, Y. Yu, Enzyme-instructed self-aggregation of Fe3O4 nanoparticles for enhanced MRI T2 imaging and photothermal therapy of tumors, Nanoscale 12 (2020) 1886–1893, https://doi.org/10.1039/c9nr09235h.
[27] R. Megías, M. Arco, J. Ciriza, L. Saenz Del Burgo, G. Puras, M. López-Viota, A. V. Delgado, J.P. Dobson, J.L. Arias, J.L. Pedraz, Design and characterization of a magnetite/PEI multifunctional nanohybrid as non-viral vector and cell isolation system, Int. J. Pharm. 518 (1–2) (2017) 270–280, https://doi.org/10.1016/j.ijpharm.2016.12.042.
[28] R.S. Sari, A.C. Almeida, A.S.R. Cangussu, J. Edson, O.D. Mozzer, H.O. Santos, W. Quintilio, I. Viana, V. Aguiar, A.M. Samir, E.M. Sobrinho, Anti-botulism single-shot vaccine using chitosan for protein encapsulation by simple coacervation, Anaerobe 42 (2016) 182–187, https://doi.org/10.1016/j.anaerobe.2016.10.013.
[29] J. Keyvan Rad, Z. Alinejad, S. Khoei, A.R. Mahdavian, Controlled release and photothermal behavior of multipurpose nanocomposite particles containing encapsulated gold-decorated magnetite and 5-FU in poly (lactide-co-glycolide), ACS Biomater. Sci. Eng. 5 (2019) 4425–4434, https://doi.org/10.1021/acsbiomaterials.9b00790.
[30] C.J. Van Oss, Interfacial Forces in Aqueous Media, second ed., CRC Press, Boca Raton, Florida, 2006.
[31] L.H. Reddy, J.L. Arias, J. Nicolas, P. Couvreur, Magnetic nanoparticles: design and characterization, toxicity and biocompatibility, pharmaceutical and biomedical

applications, Chem. Rev. 112 (2012) 5818–5878, https://doi.org/10.1021/cr300068p.
[32] A. Qureashi, A.H. Pandith, A. Bashir, T. Manzoor, L.A. Malik, F.A. Sheikh, Citrate coated magnetite: a complete magneto dielectric, electrochemical and DFT study for detection and removal of heavy metal ions, Surface. Interfac. 23 (2021) 101004, https://doi.org/10.1016/j.surfin.2021.101004.
[33] J.L. Arias, L.H. Reddy, P. Couvreur, Fe3O4/chitosan nanocomposite for magnetic drug targeting to cancer, J. Mater. Chem. 22 (2012) 7622–7632, https://doi.org/10.1039/C2JM15339D.
[34] F. Reyes-Ortega, Á.V. Delgado, E.K. Schneider, B.L.C. Fernández, G.R. Iglesias, Magnetic nanoparticles coated with a thermosensitive polymer with hyperthermia properties, Polymers 10 (2017) 10, https://doi.org/10.3390/polym10010010.
[35] B. Sanz, M.P. Calatayud, N. Cassinelli, M.R. Ibarra, G.F. Goya, Long-term stability and reproducibility of magnetic colloids are key issues for steady values of specific power absorption over time, Eur. J. Inorg. Chem. 2015 (2015) 4524–4531, https://doi.org/10.1002/ejic.201500303.
[36] A. Cenalmor, E. Pascual, S. Gil-Manso, R. Correa-Rocha, J.R. Suárez, I. García-Álvarez, Evaluation of anti-neuroinflammatory activity of isatin derivatives in activated microglia, Molecules 28 (2023) 4882, https://doi.org/10.3390/molecules28124882.
[37] B.C. Dash, G. Réthoré, M. Monaghan, K. Fitzgerald, W. Gallagher, A. Pandit, The influence of size and charge of chitosan/polyglutamic acid hollow spheres on cellular internalization, viability and blood compatibility, Biomaterials 31 (2010) 8818—8197, https://doi.org/10.1016/j.biomaterials.2010.07.067.
[38] R. Stein, B. Friedrich, M. Mühlberger, N. Cebulla, E. Schreiber, R. Tietze, I. Cicha, C. Alexiou, S. Dutz, A.R. Boccaccini, H. Unterweger, Synthesis and characterization of citrate-stabilized gold-coated superparamagnetic iron oxide nanoparticles for biomedical applications, Molecules 25 (2020) 4425, https://doi.org/10.3390/molecules25194425.
[39] M.A. Gonzalez-Fernandez, T.E. Torres, M. Andrés-Vergés, R. Costo, P. de la Presa, C.J. Serna, M.P. Morales, C. Marquina, M.R. Ibarra, G.F. Goya, Magnetic nanoparticles for power absorption: optimizing size, shape and magnetic properties, J. Solid State Chem. 182 (2009) 2779–2784, https://doi.org/10.1016/j.jssc.2009.07.047.
[40] S. Campelj, D. Makovec, M. Drofenik, Preparation and properties of water-based magnetic fluids, J. Condens. Matter Phys. 20 (2008) 204101, https://doi.org/10.1088/0953-8984/20/20/204101.
[41] L. Chekli, S. Phuntsho, M. Roy, E. Lombi, E. Donner, H.K. Shon, Assessing the aggregation behaviour of iron oxide nanoparticles under relevant environmental conditions using a multi-method approach, Water Res. 47 (2013) 4585–4599, https://doi.org/10.1016/j.jclepro.2013.04.029.
[42] S. Bhattacharjee, DLS and zeta potential - what they are and what they are not? J. Contr. Release 235 (2016) 337–351, https://doi.org/10.1016/j.jconrel.2016.06.017.
[43] J. Lim, S.P. Yeap, H.X. Che, S.C. Low, Characterization of magnetic nanoparticle by dynamic light scattering, Nanoscale Res. Lett. 8 (2013) 1–14, https://doi.org/10.1186/1556-276X-8-381.
[44] S. Eliyahu, A. Almeida, M.H. Macedo, J. das Neves, B. Sarmento, H. Bianco-Peled, The effect of freeze-drying on mucoadhesion and transport of acrylated chitosan nanoparticles, Int. J. Pharm. 573 (2020) 118739, https://doi.org/10.1016/j.ijpharm.2019.118739.
[45] T. Zelenková, R. Onnainty, G.E. Granero, A.A. Barresi, D. Fissore, Use of microreactors and freeze-drying in the manufacturing process of chitosan coated PCL nanoparticles, Eur. J. Pharmaceut. Sci. 119 (2018) 135–146, https://doi.org/10.1016/j.ejps.2018.04.006.
[46] W. Abdelwahed, G. Degobert, S. Stainmesse, H. Fessi, Freeze-drying of nanoparticles: formulation, process and storage considerations, Adv. Drug Deliv. Rev. 58 (2006) 1688–1713, https://doi.org/10.1016/j.addr.2006.09.017.
[47] L.P. Ferreira, C.P. Reis, T.T. Robalo, M.E. Melo Jorge, P. Ferreira, J. Gonçalves, A. Hajalilou, M.M. Cruz, Assisted synthesis of coated iron oxide nanoparticles for magnetic hyperthermia, Nanomaterials 12 (2022) 1870, https://doi.org/10.3390/nano12111870.
[48] R.C. Plaza, J.L. Arias, M. Espín, M.L. Jiménez, A.V. Delgado, Aging effects in the electrokinetics of colloidal iron oxides, J. Colloid Interface Sci. 245 (2002) 86–90, https://doi.org/10.1006/jcis.2001.7964.
[49] G.R. Iglesias, F. Reyes-Ortega, B.L. Checa-Fernandez, A.V. Delgado, Hyperthermia-triggered gemcitabine release from polymer-coated magnetite nanoparticles, Polymers 10 (2018) 269, https://doi.org/10.3390/polym100302969.
[50] M. Ziegler-Borowska, D. Chełminiak, H. Kaczmarek, A. Kaczmarek-Kędziera, Effect of side substituents on thermal stability of the modified chitosan and its nanocomposites with magnetite, J. Therm. Anal. Calorim. 124 (2016) 1267–1280.
[51] H. Paula, R. Silva, C.M. Santos, F. Dantas, R. de Paula, L. de Lima, E.F. de Oliveira, E. Figuereido, F. Días, Eco-friendly synthesis o fan alkyl chitosan derivative, Int. J. Biol. Macromol. 163 (2020) 1591–1598, https://doi.org/10.1016/j.ijbiomac.2020.08.058.
[52] R.J.P. Lyon, Infrared absorption spectroscopy, in: J. Zussman (Ed.), Physical Methods, in Determinative Mineralogy, Academic Press, London, 1967, pp. 371–399.
[53] R.M. Cornell, U. Schwertmann, The Iron Oxides: Structure, Properties, Reactions, Occurences and Uses, Wiley-VCH, Weinheim, 2003.
[54] R. Hergt, S. Dutz, Magnetic particle hyperthermia-biophysical limitations of a visionary tumour therapy, J. Magn. Magn Mater. 311 (2007) 187–192, https://doi.org/10.1016/j.jmmm.2006.10.1156.
[55] A. Bucharskaya, G. Maslyakova, G. Terentyuk, A. Yakunin, Y. Avetisyan, O. Bibikova, E. Tuchina, B. Khlebtsov, N. Khlebtsov, V. Tuchin, Towards effective photothermal/photodynamic treatment using plasmonic gold nanoparticles, Int. J. Mol. Sci. 17 (2016) 1295, https://doi.org/10.3390/ijms17081295.
[56] S. Dutz, R. Hergt, Magnetic particle hyperthermia—a promising tumour therapy? Nanotechnology 25 (45) (2014) 452001 https://doi.org/10.1088/0957-4484/25/45/452001.
[57] J. Faraudo, J.S. Andreu, J. Camacho, Understanding diluted dispersions of superparamagnetic particles under strong magnetic fields: a review of concepts, theory and simulations, Soft Matter 9 (2013) 6654–6664, https://doi.org/10.1039/C3SM00132F.
[58] I. Conde-Leboran, D. Baldomir, C. Martinez-Boubeta, O. Chubykalo-Fesenko, M. del Puerto Morales, G. Salas, D. Serantes, A single picture explains diversity of hyperthermia response of magnetic nanoparticles, J. Phys. Chem. C 119 (27) (2015) 15698–15706, https://doi.org/10.1021/acs.jpcc.5b02555.
[59] J.G. Ovejero, D. Cabrera, J. Carrey, T. Valdivielso, G. Salas, F.J. Teran, Effects of inter-and intra-aggregate magnetic dipolar interactions on the magnetic heating efficiency of iron oxide nanoparticles, Phys. Chem. Chem. Phys. 18 (16) (2016) 10954–10963, https://doi.org/10.1039/c6cp00468g.
[60] S. Jeon, B.C. Park, S. Lim, H.Y. Yoon, Y.S. Jeon, B.S. Kim, Y.K. Kim, K. Kim, Heat-generating iron oxide multigranule nanoclusters for enhancing hyperthermic efficacy in tumor treatment, ACS Appl. Mater. Interfaces 12 (2020) 33483–33491, https://doi.org/10.1021/acsami.0c07419.
[61] S. Shen, S. Wang, R. Zheng, X. Zhu, X. Jiang, D. Fu, W. Yang, Magnetic nanoparticle clusters for photothermal therapy with near-infrared irradiation, Biomaterials 39 (2015) 67–74, https://doi.org/10.1016/j.biomaterials.2014.10.064.
[62] R. Ge, X. Li, M. Lin, D. Wang, S. Li, S. Liu, Q. Tang, Y. Liu, J. Jiang, L. Liu, H. Sun, H. Zhang, B. Yang, Fe3O4@polydopamine composite theranostic superparticles employing preassembled Fe3O4 nanoparticles as the core, ACS Appl. Mater. Interfaces 8 (2016) 22942–22952, https://doi.org/10.1021/acsami.6b07997.
[63] S. Vaezifar, S. Razavi, M.A. Golozar, S. Karbasi, M. Morshed, M. Kamali, Effects of some parameters on particle size distribution of chitosan nanoparticles prepared by ionic gelation method, J. Cluster Sci. 24 (2013) 891–903, https://doi.org/10.1007/s10876-013-0583-2.
[64] E.T. Sarcan, M. Silindir-Gunay, A.Y. Ozer, Theranostic polymeric nanoparticles for NIR imaging and photodynamic therapy, Int. J. Pharm. 551 (2018) 329–338, https://doi.org/10.1016/j.ijpharm.2018.09.019.